Particle Reduced, Efficient Gasoline Engines

EUROPEAN COMMISSION
Horizon 2020 | GV-2-2016 | Technologies for low emission light duty powertrains
GA # 723954

Deliverable No.	PaREGEn D1.6 Work Package 1: Advanced Combustion Technologies	
Deliverable Title	Report on optical diagnostics for fuel films, mixture inhomogeneities, soot and water injection in optical engines. Focus is on implications for models for design and control.	
Deliverable Date	2019-04-30	
Deliverable Type	REPORT	
Dissemination level	Public (PU)	
Written By	Niklas Jüngst (UDE) Sebastian Kaiser (UDE)	2019-04-10 2019-04-10
Checked by	Andreas Manz (Bosch)	2017-04-10
Approved by	Sebastian Kaiser (UDE) Andreas Manz (Bosch) Jens Ewald (FEV) Simon Edwards (RIC) - Coordinator	2017-04-10 2017-04-10 2017-04-29 2017-04-30
Status	Final	2017-04-30

Summary

Late-evaporating liquid fuel wall films are considered a major source of soot in gasoline direct-injection (DI) engines. In this study, a DI model experiment was developed to visualize soot formation in the vicinity of evaporating fuel films. Isooctane is injected by a multi-hole injector into a wind tunnel with an optically accessible test section. For fuel-film imaging, a mixture of isooctane (surrogate fuel) and toluene (fluorescent tracer) is used as the fuel. Air flows continuously at low speed and ambient pressure through the test section. Some of the liquid fuel impinges on the quartz-glass windows and forms fuel films. After spark ignition, a turbulent flame front propagates through the chamber and ignites pool fires near the fuel films, leading to locally sooting combustion. Laser-induced fluorescence (LIF) of toluene using 266 nm excitation images the fuel-film thickness and the fuel vapour above the liquid films. A laser light-sheet with a wavelength 532 nm excites LIF of large polycyclic aromatic hydrocarbons (PAH) with five or more aromatic rings, considered as soot precursors, near the evaporating fuel films. Additionally, a light sheet at 1064 nm excites laser-induced incandescence (LII) of soot particles. Two intensified CCD cameras simultaneously detect the LII and LIF signals, and thus visualize PAH and soot. In complementary line-of-sight imaging, the fuel spray, chemiluminescence of the flame, and soot incandescence are captured with a high-speed colour camera. In addition to this fuel-injection experiment, a sooting laminar coflow flame burning ethylene in air ("Santoro burner") is used for preliminary in-situ measurements.

The tracer-LIF images show that indeed the fuel wall-films remain on the surface long after the flame front has passed, leading to inhomogeneities in the fuel/air-mixture. The evaporation of individual fuel films was investigated for different injection masses, wall temperatures, flow velocities, and also under the influence of combustion. In general, the evaporation rate is highest shortly after the end of injection when the strong turbulence, induced by the injection event, enhances the mass transport of liquid fuel into the gas phase. Beyond that time, the results show that the wall temperature has the largest influence on the fuel-film evaporation rate, indicating that the conductive heat flux from the wall determines the evaporation.

Results from simultaneous imaging of PAH LIF and soot LII show soot to occur mostly spatially separated from the PAH and with high spatial intermittency. Images from high-speed imaging visualize the flame front and soot luminosity and show that the latter is detected in similar regions as soot LII. The chemiluminescence indicates oxidation of soot and PAH as they are being transported downstream. PAH and soot are detected as sharp filaments near the fuel films mostly spatially separated from each other. In a given snapshot, either soot or PAH or both are detected near the fuel films, indicating that the two species do not need to appear together every time.

The methods developed in Subtasks 1.3.1, diagnostics for fuel films, and 1.3.3, diagnostics for combustion, soot, and soot precursors, are currently being utilized in an optically accessible research engine at BOSCH. Results on quantitative fuel-film imaging in that engine have already been reported in Deliverable 1.2 and in a peer-reviewed publication [1]. Also, results of fuel-film evaporation, soot and soot precursors obtained from the DI model experiment in the wind tunnel are used as validation data for 3D simulations in Task 1.4, by the project partners ETH, BOSCH, and LOGE. In particular, ETH has simulated the fuel-film evaporation and found results that were consistent with the experiments. A simulation of combustion, formation of soot precursors soot ongoing work there. Experiments with endoscopic imaging at BOSCH, Subtask 1.3.4, are planned for June 2019, while work on infrared-absorption of water imaging in the optical engine (part of Subtask 1.3.2) has been rescheduled for Q3 2019. Some of the work reported here has been presented at SAE WCX 2019 and is published as SAE Technical Paper 2019-01-0293.

Contents

Figures

Tables

1 Introduction

Injecting the liquid fuel directly into the combustion chamber can provide high efficiency, performance, and knock suppression in gasoline spark-ignition engines. However, under some conditions injected fuel may wet in-cylinder surfaces, and if the fuel in these films does not evaporate and mix sufficiently with air before combustion, the resulting inhomogeneities of the fuel/air-mixture make the formation of polycyclic aromatic hydrocarbons (PAH) and soot likely. Laser diagnostics are promising tools to investigate the sub-processes in soot formation, such as spray, fuel-film formation, evaporation, mixture formation, ignition and combustion.

The correlation between fuel films on the piston and the engine-out soot emissions was investigated by Warey *et al.* [2], Drake *et al.* [3], Ortmann *et al.* [4] and Stevens *et al.* [5]. Warey *et al.* measured particulate mass and size distributions stemming from piston fuel-films for different fuels [2]. Drake *et al*. imaged the thickness of evaporating fuel films by refractive index matching (RIM) and identified pool fires above those seen with high-speed imaging of the combustion luminosity in an optically accessible direct-injection spark-ignition (DISI) engine [3]. They found the first soot formation from fuel-rich pockets soon after the spark. However, most of this soot was oxidized in the cylinder during the remainder of the cycle. In contrast, soot formed in pool fires was not burned out due to low turbulent mixing rates and low temperatures close to the walls and was detected in some cycles until exhaust valve opening. By simultaneously imaging OH* chemiluminescence (CL) and laser-induced incandescence (LII) of soot, Stojkovic *et al.* [6] also revealed two distinct stages of soot formation in a DISI engine operating with a stratified fuel/air-mixture. They found that early soot originates from regions with partially premixed combustion close to the electrodes, indicated by OH*-CL, and is oxidized later due to high temperatures (2000 - 2400 K) and turbulent mixing. Soot formation from pool fires occurs later and becomes significant when 80% of the heat has already been released. Temperatures then are much lower (about 1700 K), such that oxidation is unlikely, causing persistent soot and engine-out emissions. In a wall-guided gasoline direct injection (GDI) engine, Ortmann *et al.* visualized the formation of fuel films and measured the engine-out emissions of soot and unburned hydrocarbons [4]. Stevens et al. used laser-induced fluorescence (LIF) to show that for late injection, where the piston is close to the injector, significant amounts of fuel impinge on the piston [5]. High-speed imaging of the flame luminosity revealed that under these conditions pool fires may exist into the exhaust stroke because there is not enough time for film evaporation. When fuel films persist into the exhaust stroke and the local temperature is too low to cause soot formation, unburned hydrocarbons are emitted [7-10]. Recently, Schulz *et al*. investigated the effect of rail and ambient pressure on the evaporation duration of liquid fuel films in a pressure vessel by high-speed visualization [11].

To investigate the impact of evaporating fuel films in combustion as a source of soot formation, instantaneous two-dimensional detection of the film thickness is desirable. Candidate techniques for the imaging of thin liquid films are RIM and LIF. In RIM, a roughened transparent surface, such as a quartz window, is illuminated from the bottom and the backscattered light is captured with a camera. When a liquid, such as fuel, adheres to the top of the rough surface, the change in the refractive index and hence the intensity of backscattered light is less than when no fuel adheres to the surface. However, at a certain thickness the technique becomes insensitive to thickness because the film covers the surface roughness and no scattered light is detected anymore [3]. Typical detectable thicknesses are in the range of 0.03 to 3 µm. Maligne and Bruneaux compared the measured fuel-film thicknesses from RIM and LIF (see below) and found them to be in a good agreement [12].

Quantitative imaging of the film thickness with LIF requires the use of a fluorescent tracer added to a liquid surrogate fuel in small concentration. By judicious choice of the tracer concentration the dynamic range of the experiment can be adjusted to the expected range of film thicknesses. Quantitative LIF fuel-film imaging on the piston window of an optical DISI engine was recently performed by Geiler *et al.* [1].

As the fuel films evaporate, inhomogeneities in the fuel/air-mixture arise near the films. The visualization of the nearby gaseous fuel is desirable, since soot formation is most likely in these regions. Tracer LIF imaging of the gas phase is much more common than of the liquid phase, and overviews of the technique can be found in [13] and comparisons of the photophysical properties of selected tracers in [14, 15].

When the premixed flame front reaches the inhomogeneous fuel/air-mixture near the fuel films, it may turn into a non-premixed flame, producing soot. Laser-induced incandescence (LII) and high-speed combustion imaging are techniques for the visualization of soot. In LII a high energy laser pulse heats soot to temperatures high above flame temperatures, leading to an intense broadband emission according to Planck's law. The LII signal is detected point-wise or 2D and gives relative soot concentrations or soot volume fractions after calibration. Bockhorn investigated the formation and oxidation of soot in detail [16]. So far, the investigation of soot formation in internal combustion engines focused mainly on Diesel. The diffusion-controlled combustion is likely for the formation of undesired soot particles from local inhomogeneities in the air-fuel mixture. Notably, Dec et al. investigated the soot formation in Diesel engines with 2-D imaging of soot by LII [17, 18]. Dec came up with a conceptual model of the different combustion stages [19]. The formation of soot from diffusion flames in a gasoline direct injection (GDI) engine, in particular from pool fires, is barely understood. Two-dimensional soot volume fraction measurements [20] and particle size measurements [21] were carried out in GDI engines by means of LII. Francqueville et al. measured soot volume fractions in a spray-guided DISI engine and observed a sharp decrease of the soot concentration during the expansion stroke, most likely due to oxidation.

Deriving the cause and effect relationship in soot formation from fuel films requires an understanding of the formation of soot precursors, polycyclic aromatic hydrocarbons. In aliphatic flames, the fuel first decomposes into polyacetylenes, such as ethylene, methyl radicals and other species. Free-radical chain-lengthening reactions lead to the formation of long C_4, C_6, and C_8-species. Those form aromatic species, which contain a benzene ring, by cyclisation reactions. These grow further due to the collision with acetylene species (HACA-mechanism). When they consist of at least two benzene rings, they are known as polycyclic aromatic hydrocarbons (PAH) [22]. A species selective measurement of PAH is possible with ex-situ techniques like photoionization coupled with mass spectrometry or jet-cooled laser-induced fluorescence [23, 24] [25]. However, many PAH exhibit broadband optical absorption and fluorescence properties, which makes them, in particular in turbulent environments, favourable for non-intrusive in-situ measurements [26]. When PAH are increasing in number of benzene rings, their absorption spectrum shifts to longer wavelengths, so as the subsequent fluorescence. This allows for a size-dependent detection of PAH based on the excitation wavelength [25]. Exemplarily at flame temperature, PAH containing more than five aromatic rings absorb and fluoresce in the visible while smaller PAH absorb and fluoresce in the UV [25]. The high number of different PAH, their different spectroscopic properties and the dependency of those on temperature and the collision quenching environment make a quantification of PAH concentration based on LIF impossible [23],[25]. Bejaoui *et al.* collected spectra of PAH in premixed and diffusion flames after excitation, ranging from 266 to 680 nm. They found that when exciting in the UV, fluorescence spectra from the diffusion flame shifted about 50 nm to the red while there was no spectral shift in the premixed flame with increasing height above the nozzle (HAB). This indicates the stratification of PAH in the diffusion flame with increasing HAB and that many different size classes of PAH are excited in the UV. Extending the excitation wavelength from 415 nm to 680 nm shifts the full width half maximum (FWHM) about 100 nm to the red. Also, excitation in the visible did not show any shift to longer wavelengths with increasing HAB, indicating a limited pool of PAH being excited in the visible (only PAH with more than four benzene rings [27]) [24]. Schoemacker *et al.* investigated soot formation in a diffusion flame by visualizing PAH and soot simultaneously, excited at 532 and 1064 nm, respectively [28]. Lemaire *et al.* found soot precursors and soot spatially well separated in a turbulent diffusion flame [29]. Hayashida *et al.* simultaneously visualized OH, PAH and soot, excited at 248 nm, in a laminar propane diffusion flame [30]. PAH-LIF was detected in the fuel region and LII further downstream of the flame. A minimum in the signal along the burner axis indicated the soot inception region. Also, Vander Wal *et al.* visualized both PAH-LIF and LII of soot and indicated a "dark zone" between PAH and

soot in a laminar diffusion flame [31]. The growth of PAH was visualized by increasing the excitation wavelength from 266 to 532 and 633 nm in an optically accessible diesel engine by Musculus *et al.* [32]. Simultaneously the laser-induced incandescence, excited at 1064 nm, reveals the soot inception regions. Combining PAH LIF and soot LII with imaging natural flame luminosity was barely done. Smyth *et al.* have imaged broadband fluorescence and visible flame luminosity in hydrocarbon diffusion flames to identify soot oxidation regions [33]. Also Oliveira *et al.* imaged the nucleation of PAH to soot [34]. Recently Hayashi *et al.* published a study on simultaneous imaging of Mie scattering PAH-LIF and soot LII in a small scale pulverized coal flame [35]. They found PAHs and soot spatially well separated from each other in instantaneous measurements and also that PAH mostly form in the premixed flame structure region while soot is present in the diffusion flame region [35].

In this work simultaneous imaging of PAH LIF, excited at 532 nm, and soot LII, excited at 1064 nm, is done to visualize the soot formation process in the vicinity of evaporating fuel films. High-speed colour combustion-imaging is done in a separate experiment to visualize the flame front, natural flame luminosity, and soot oxidation regions.

Preliminary experiments on an imaging diagnostic visualizing the water injection in the cylinder or the port via infrared (IR) absorption have already been reported in D1.5. While no major obstacles are expected, the diagnostic has not yet been applied in the optical engine, as originally planned, because the development of the diagnostics for fuel films, soot, and soot precursors was more complex than anticipated. However, experiments on IR-absorption imaging of water injection in the optical engine at BOSCH are planned for Q3 2019.

2 Development of optical diagnostics

Laser diagnostics for fuel-film, fuel-vapour, soot, and soot precursor imaging are described in this chapter. The diagnostics are developed in a wind tunnel with an optically accessible test section, which is considered as a direct-injection model experiment. Optical layouts for complementary line-of-sight imaging, schlieren- and high-speed colour combustion-imaging, are also shown. It needs to be taken into account that fuel-vapour and schlieren imaging were done with an injector other than the project injector. Fuel-vapour imaging will be done with the project injector in July 2019.

2.1 Flow facility

A sketch of the DISI model experiment, the optically accessible test section of a wind tunnel, is shown in Figure 1. The test section of our tunnel consists of three quartz walls that provide optical access. An injector and spark electrodes protrude through an aluminium plate, the fourth wall of the section.

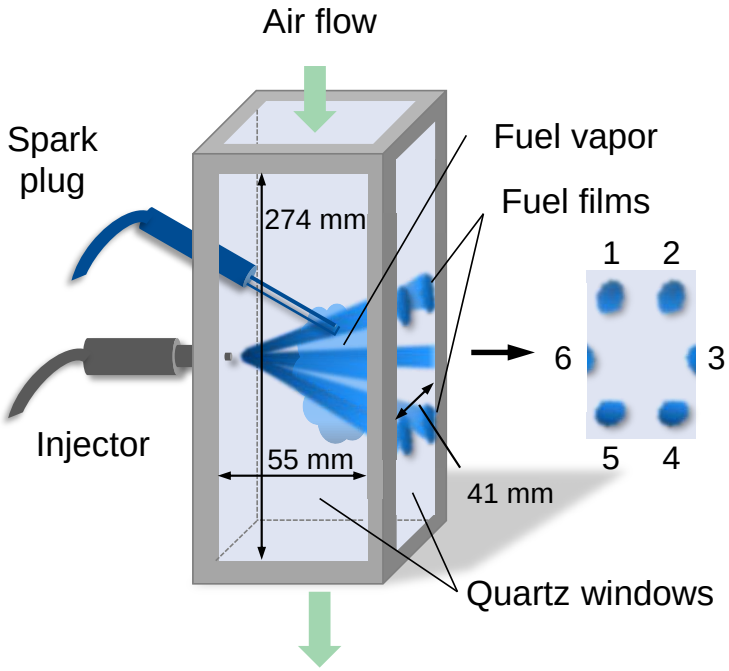

Figure 1: (left) Optically accessible test section of wind tunnel with injector and spark electrodes. (right) Numbering of the six fuel films.

Heated air flows continuously from the top to bottom with a nominal velocity of 2.23 m/s. A perforated plate stacked with fine wire meshing is located between the air heater and the test section to provide small-scale turbulence and a uniform bulk flow. A six-hole nozzle injects fuel evaporating into the hot air flow. Some of the injected fuel wets the quartz wall on the opposite side. Fuel films 1 (topmost) and 4 (bottommost) lie completely on the quartz wall, as indicated in Figure 1. The remaining four spray cones impinge mainly on the metal frame next to the quartz window. Thus, fuel films 2, 3, 5, and 6 lie only to small extent on the quartz wall. The impingement distance (the distance between the nozzle tip and the wall along the jet axis) is approximately 50 mm for fuel film 1. This distance yields a reproducible ignition of the fuel/air-mixture in every injection event. A pair of electrodes below the injector (see Fig. 1) ignites the fuel/air-mixture 1 ms after the end of injection (EOI). Therefore, the experiment employs a combination of a spray-guided and wall-guided direct-injection strategy. The latter is known to potentially lead to increased soot formation [36]. Table 1 gives an overview of the operating conditions in the experiments. Parameters that were varied in the experiments are the air temperature and the injection duration (and thus the injected mass). The air, wall, and injector temperatures cannot be controlled independently but follow the air temperature as given in Table 1. The flow was weakly turbulent.

Table 1: Operating conditions.

Fuel	Iso-octane + 1%/ 10% toluene
Injector	Six holes
Rail pressure	100 bar
Injector temperature	361 K (339 K, 350 K)
Injection duration	0.5 ms (5 mg), 1 ms (9.3 mg)
Air temperature	381 K (340 K, 361 K)
Air flow velocity	1.8 m/s (3 m/s, 6.5 m/s, 10 m/s)
Back pressure	1 bar
Quartz wall temperature	352 K (332 K, 342 K)

After preliminary experiments, a conventional spark plug was replaced by two thin electrodes, as shown in Figure 1, disturbing the flow and obscuring the view less. This model experiment has some of the salient features of DISI engine combustion but is also simplified and thus less realistic in others. While air flow velocity and pressure vary in a real DISI engine, both are on average lower and constant in our model experiment. The temperature range was chosen to investigate the evaporation of the fuel film on a wall with a temperature below the liquid's boiling point and to investigate how sensitively it reacts to variations in the temperature. Since piston temperatures might be higher in a DISI engine, and the pressures are, the fuel temperature is most presumably also below the liquid's boiling point.

2.2 LIF for liquid-film imaging

The absorption of light is described by the Beer-Lambert law [37],

$$I_t = I_0 \cdot e^{-(\varepsilon^* \cdot c \cdot d)} \tag{1}$$

Here, I_t denotes the transmitted intensity, I_0 the incident intensity, ε^* the molar extinction coefficient, c the molar concentration of the absorbing species, and d the absorption path length. Therefore, the "absorbed intensity" I_a is equal to the difference between incident and transmitted intensity:

$$I_a = I_0 \cdot (1 - e^{-(\varepsilon^* \cdot c \cdot d)}) \tag{2}$$

The absorption of light by a molecule can promote an electron from the ground level to a higher energy level. In the conditions considered here, within that excited electronic state the molecule quickly relaxes to vibrational and rotational equilibrium. When the electron returns to the ground state, the remaining energy may be released by the emission of a photon, a process known as a fluorescence [38].

The detected fluorescence intensity is proportional to the absorbed intensity, the fluorescence quantum yield (FQY), $\phi = \left(\frac{\#\ photons\ emitted}{\#\ photons\ absorbed}\right)$, and the collection and detection efficiency $\Omega \cdot \eta$ of the imaging system [39]:

$$I_\mathrm{f} = \phi \cdot \Omega \cdot \eta \cdot I_\mathrm{a} \tag{3}$$

Combining Equations (2) and (3), the fluorescence intensity is given by

$$I_f = \phi \cdot \Omega \cdot \eta \cdot I_0 \cdot (1 - e^{-(\varepsilon^* \cdot c \cdot d)}). \quad (4)$$

When the exponent in Equation (4) is small, the fluorescence intensity is in good approximation proportional to the concentration of the fluorescing species and the absorption path length:

$$I_f = \phi \cdot \Omega \cdot \eta \cdot I_0 \cdot \varepsilon^* \cdot c \cdot d \quad (5)$$

2.3 Optical diagnostics

2.3.1 Tracer

Commercial fuels contain many different components that fluoresce when excited by UV lasers. All of them exhibit different photophysical properties, meaning that the signal of each component individually depends on temperature, pressure, and bath gas composition. Hence it is impossible to derive quantitative information, such as species concentration, from the total detected signal, which is an overlap of the individual contributions. For quantitative LIF imaging of fuels, a mixture of some fluorescent marker in a non-fluorescing surrogate is usually applied [13]. As a non-fluorescing surrogate fuel iso-octane is chosen (boiling point 372 K), which is also found in commercial fuels. The fluorescent tracer, added to the surrogate fuel, should co-evaporate with the surrogate. Additionally, the tracer should exhibit similar properties in terms of droplet formation, diffusivity and convection [13]. For fuel-film imaging, it is very important that the surrogate fuel and the tracer co-evaporate so that the fraction of the tracer does not change in the liquid and gaseous fuel. Also, the spectral properties of the tracer, the dependence of the LIF-signal on temperature, pressure and bath-gas composition should be known [40]. Toluene (boiling point 384°K) fulfills these requirements mostly and is chosen as a fluorescent tracer, which is added in different concentrations to iso-octane in the experiments. Figure 2 shows the fluorescence signal of liquid toluene, excited at 266 nm. Also, the transmission curves of the longpass filter LP266 blocking the laser light, and the bandpass filter BP292 isolating the toluene fluorescence from interfering background fluorescence, are shown. For the wall-film imaging, the volume fraction of toluene in iso-octane is 1 vol.-%. Since the tracer concentration is about 2500 times lower and oxygen quenching leads to a strong signal decrease in fuel-vapour imaging, the volume fraction is chosen as 10 vol.-%.

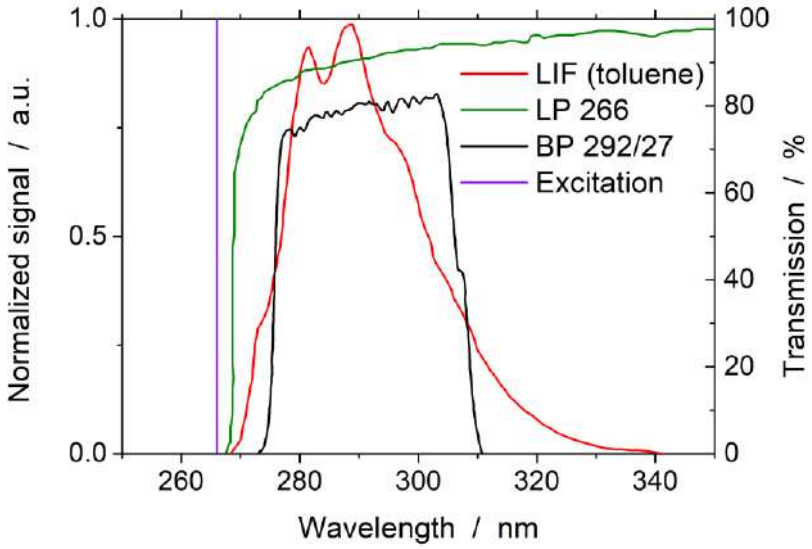

Figure 2: Fluorescence spectrum of liquid toluene, excited at 266 nm, and transmission of filters applied for toluene LIF.

2.3.2 Fuel-film imaging

The experiment for fuel-film imaging is shown in Figure 3. A Pellin-Broca prism separated the fourth harmonic (266 nm) from an Nd:YAG laser (Litron Nano L PIV Series) from the remaining second harmonic (532 nm). The pulse energy was adjusted by a dielectric beam attenuator. A quartz wedge reflected some portion of the laser light to an energy monitor to account for shot-to-shot fluctuations in energy. Two UV mirrors deflected the beam towards the test section. A negative spherical lens (f = -100 mm) and a negative cylindrical lens (f = -120 mm) expanded the beam vertically and horizontally. An aperture clipped the UV laser so that only the region of interest of the quartz wall was illuminated. The fluorescence was imaged by a UV lens (f = 85 mm, f/2.8) on an intensified CCD camera (LaVision), indicated by the dashed lines in Figure 3. A bandpass filter, BP 292/27 (Semrock 292/27 BrightLine HC), blocked laser stray light and spectrally further narrowed the detection region to suppress background fluorescence from the aluminium back plate of the wind tunnel, the injector tip and the electrodes. The projected pixel size was 0.09 mm/pixel. The time between two images was 2.5 seconds and hence long enough to entirely evaporate the fuel film and flush the fuel vapour from the test section, such that each image shows an individual injection at a certain time after start of injection (aSOI).

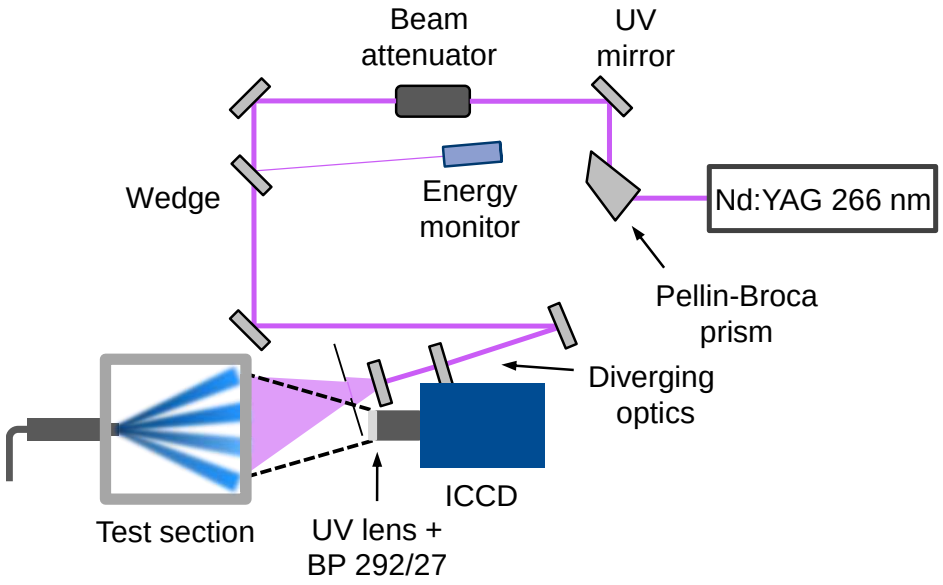

Figure 3: Optical layout for fuel-film LIF.

To account for the spatially inhomogeneous excitation, detection, and collection efficiencies in fuel-film LIF imaging, a sample was illuminated giving a uniform LIF response to laser excitation. Such a “flat-field” was acquired by illuminating a plate of quartz glass of inferior quality, which fluoresced homogeneously when excited at 266 nm. The flat-field plate was located behind the quartz wall, as indicated in Figure 4. The left image in the bottom of Figure 4, Flat-field (a), shows the LIF signal from the quartz plate when the laser light partially passes through the plate and is reflected at the aluminium back wall, where injector and electrodes were mounted. We used this flat-field to correct the fuel-film images. Since in the calibration images with a thin-film cuvette, as discussed below, these reflections do not occur, Flat-field (b) was acquired with a black background and was used to correct the calibration images. For the flat-field correction it is in particular important that both the LIF signal of toluene and the LIF signal of the flat-field material are proportional to the laser fluence. The spatial average of the laser fluence was calculated by measuring the laser pulse energy behind the aperture, indicated in Figure3, with a laser energy sensor (Coherent, J-50MB-YAG) and dividing it by the illuminated area on the quartz window. The latter was 30 cm^2 while the pulse energies were varied from 2 to 5 mJ.

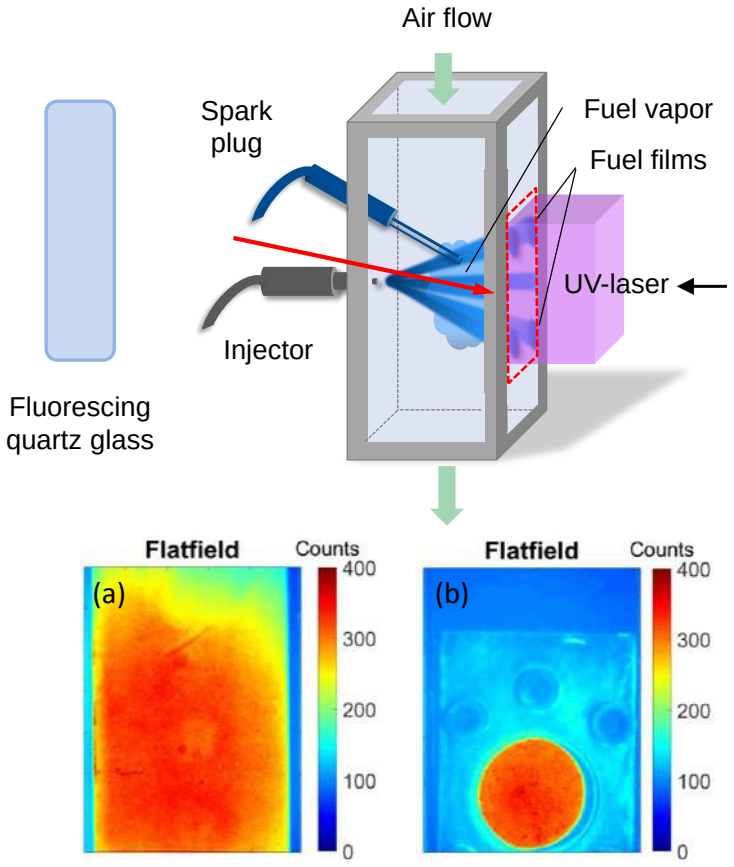

Figure 4: (top) Flat-field imaging for fuel-film LIF. (bottom) Flat-fields for (left) fuel films and (right) calibration.

Figure 5 clearly shows a linear relationship between LIF signals of toluene and the flat-field material (quartz glass of inferior quality) for the investigated laser fluence range. In the fuel-film measurements the average laser fluence was set to 0.16 mJ/cm².

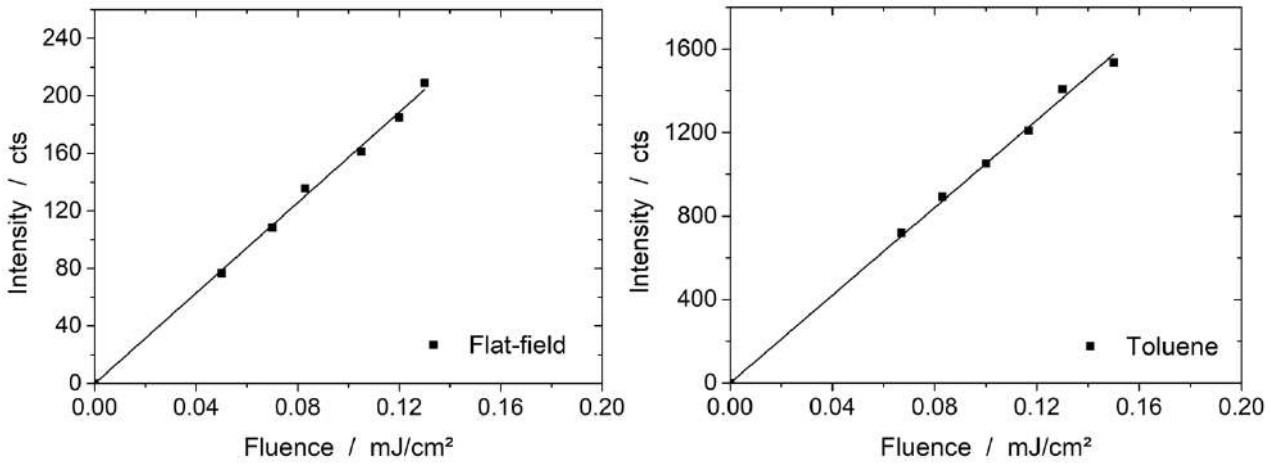

Figure 5: LIF signal versus laser fluence for (left) the flat-field material and (right) fuel film of iso-octane/toluene mixture.

For absolute calibration, fuel films with a range of thicknesses were established in a purpose-built thin-film cuvette. Precision shims created a gap of known distance between a black back wall and a quartz plate, as shown in the top left and bottom left in Figure 6. The gap was filled with the iso-octane/toluene mixture and a quartz plate pushed onto the precision shims and an O-ring (Viton gasket) surrounding the cavity by the silver holder plate. Thus, a fuel film of known thickness was created between the two shims. This calibration tool was mounted just behind the quartz-wall to perform an in-situ calibration with excitation, collection,

and detection efficiencies locally equal to those in flat-field and fuel-film imaging. The image in the bottom right of Figure 6 shows the detected LIF intensity from a fuel layer with 40 µm thickness after flat-field correction. The spatial standard deviation in the corrected image was 2.6%.

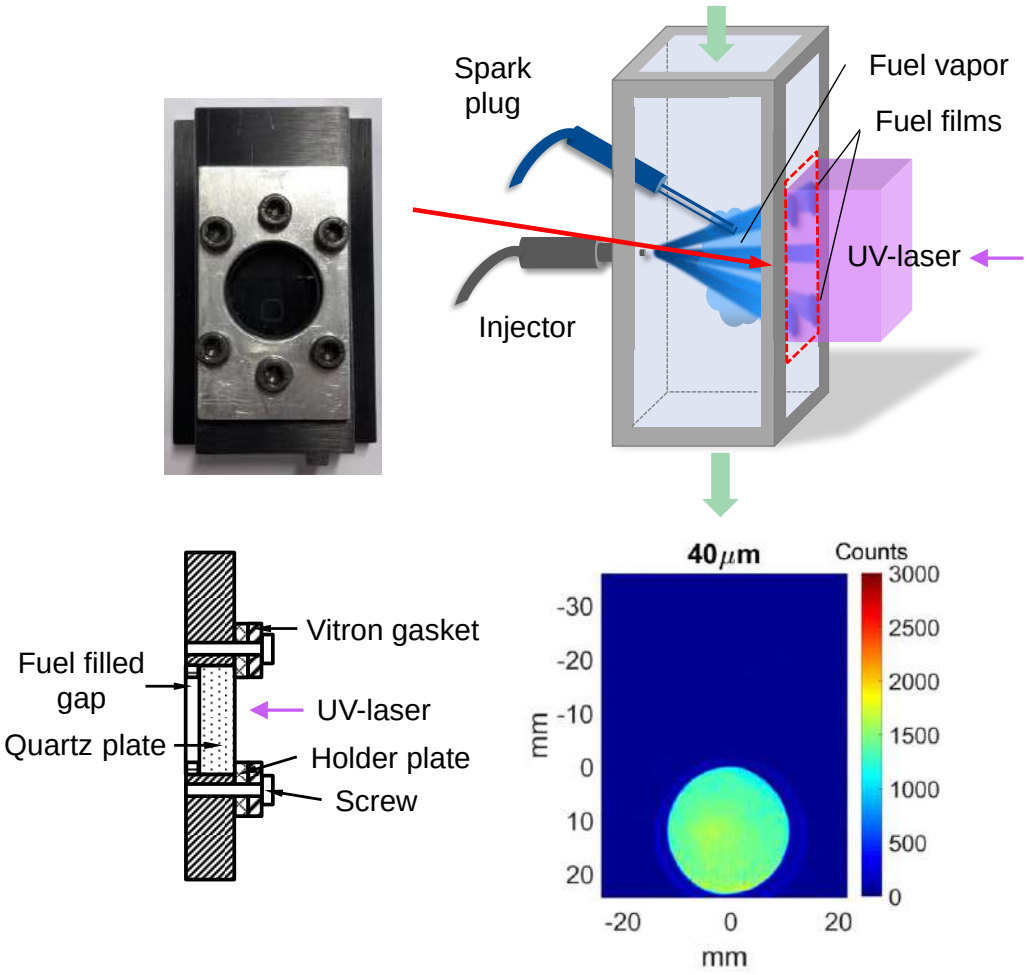

Figure 6: (top left) Calibration tool, (top right) in-situ illumination of tool, (bottom left) sectional view from the side of the calibration tool, (bottom right) resulting image for a thickness of 40 µm after background correction.

Figure 7 shows the resulting calibration function for background- and flat-field corrected LIF intensities with shim thicknesses ranging from 10 to 100 µm.

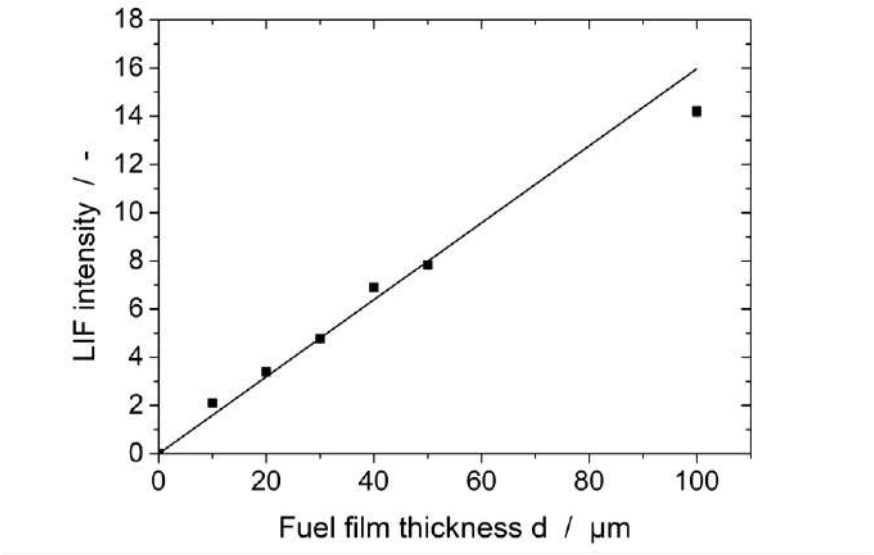

Figure 7: Calibration data of LIF signal versus fuel-film thickness. Error bars indicate the standard deviation in three individual measurements.

Each data point is the average of three individual measurements, each comprising the ensemble average of 50 background- and flat-field corrected single shots. From this ensemble average, the spatial mean in a region within the circular fuel film was calculated. In Figure 7 the deviation from the linear approximation between the LIF signal and the fuel-film thickness (Equation 5) becomes pronounced at around 100 µm.

However, measured fuel-film thicknesses did not exceed 50 µm such that the linear fit function $I_{\mathrm{f,cal}} = 0.16\frac{1}{\mu m} \cdot d_{\mathrm{cal}}$ was used to calculate the film thicknesses from the LIF signal. The fit approximates the data points very well, indicated by a coefficient of determination of 99.2%. For processing the images, each single shot was background- and flat-field corrected. With the calibration constant $\frac{d_{\mathrm{cal}}}{I_{\mathrm{f,cal}}} = 6.25$ µm the fuel film thickness was calculated pixel-wise according to:

$$d_{\mathrm{Film}}(x,y) = \frac{I_{\mathrm{f,exp}}(x,y)}{I_{\mathrm{f,cal}}} \cdot d_{\mathrm{cal}} \cdot \frac{E_{\mathrm{Reference}}}{E_{\mathrm{Measured}}} \cdot \frac{I_{\mathrm{f}}(298\ K)}{I_{\mathrm{f}}(T_{\mathrm{Wall}})} \quad (6)$$

The background and flat-field corrected fluorescence intensity of the fuel films is $I_{\mathrm{f,exp}}$, while the one in the calibration is denoted as $I_{\mathrm{f,cal}}$. The ratio $\frac{d_{\mathrm{cal}}}{I_{\mathrm{f,cal}}}$ results from the calibration function. The correction of shot-to-shot fluctuations in laser energy was accounted for by $\frac{E_{\mathrm{reference}}}{E_{\mathrm{measured}}}$. The fuel-film temperature was approximated as the quartz-wall temperature. The temperature of the injector tip, which was assumed to represent the initial fuel temperature, was about 9 K higher than the wall temperature. This would lead to a slight underprediction (maximum 8%) of the film mass at 3 ms aSOI, if the fuel had not reached the wall temperature yet. A CFD simulation by ETH in Work Package 1.4.2 shows the fuel droplets to have a temperature of 326 K at 0.5 cm before the wall. However, the fuel-film temperature is 351 K in the CFD simulation, indicating that the droplets adapt to the wall temperature quickly. Once the fuel adheres to the wall it approaches the quartz wall's temperature. Park *et al.* stated that the fuel-film temperature is about 6 K higher than the piston temperature [41]. Therefore, the acquired image was corrected by the ratio $\frac{I_{\mathrm{f}}(298\ K)}{I_{\mathrm{f}}(T_{Wall})}$, where $I_{\mathrm{f}}(298\ K)$ is the LIF signal at 298 K, and $I_f(T_{\mathrm{Wall}})$ that at quartz-wall temperature. The temperature dependence of the LIF signal of liquid toluene was measured by heating a 100 µm thick fuel film to known temperatures. Therefore, the calibration tool was put onto a plate which was heated by heating cartridges from the inside, as indicated in the top left of Figure 8. Also, a channel was drilled through the side

of the holder plate of the calibration tool into the fuel filled gap. A thermocouple, indicated by the green wire in Figure 8, was glued into the channel, measuring the temperature within the fuel filled gap. Thus, the heating cartridges were controlled in a way that the fuel film reaches the desired temperature. The fuel film of 100 µm thickness was heated to temperatures ranging from 305 to 365 K. At each temperature 100 images were acquired and ensemble averaged. The bottom of Figure 8 shows the resulting images after background correction for (left) 315 and (right) 365 K

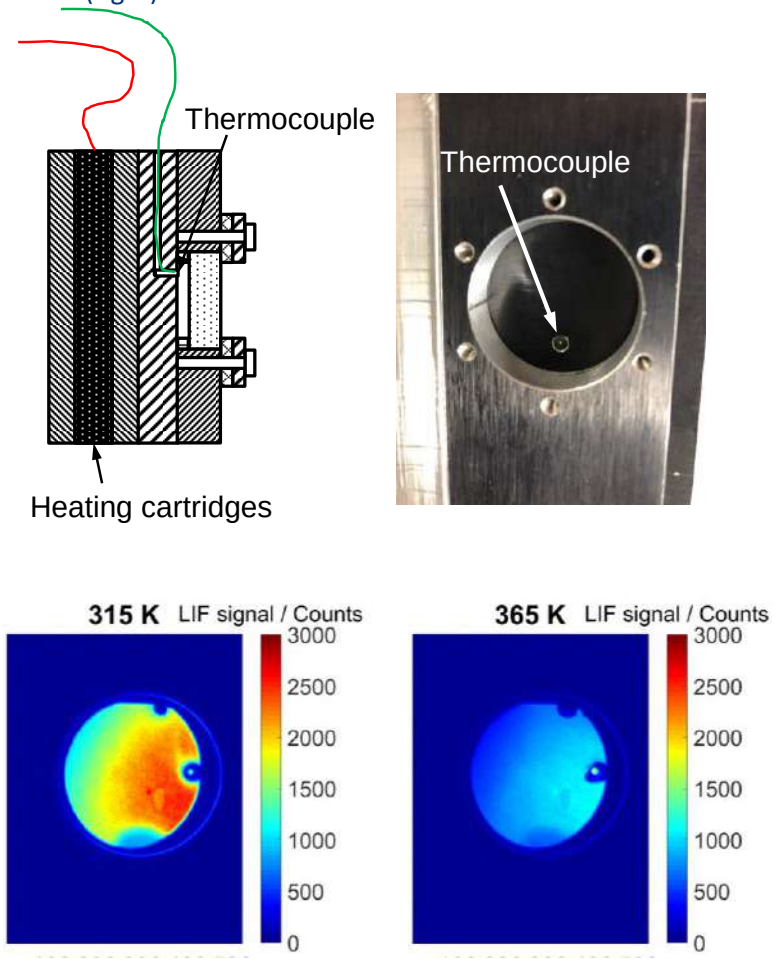

Figure 8: (top left) Sectional view of modified calibration tool with thermocouple and plate filled with heating cartridges, (top right) modified calibration tool with thermocouple in the lower region, (bottom left) resulting image of a fuel film of100 µm thickness at 315 K, (bottom right) resulting image of a fuel film of100 µm thickness at 365 K.

The signal from a region of interest was spatially averaged and plotted versus the temperature as shown in Figure 9. The result shows that the LIF signal approximately decreases linearly about a factor of 3 from 315 to 365 K.

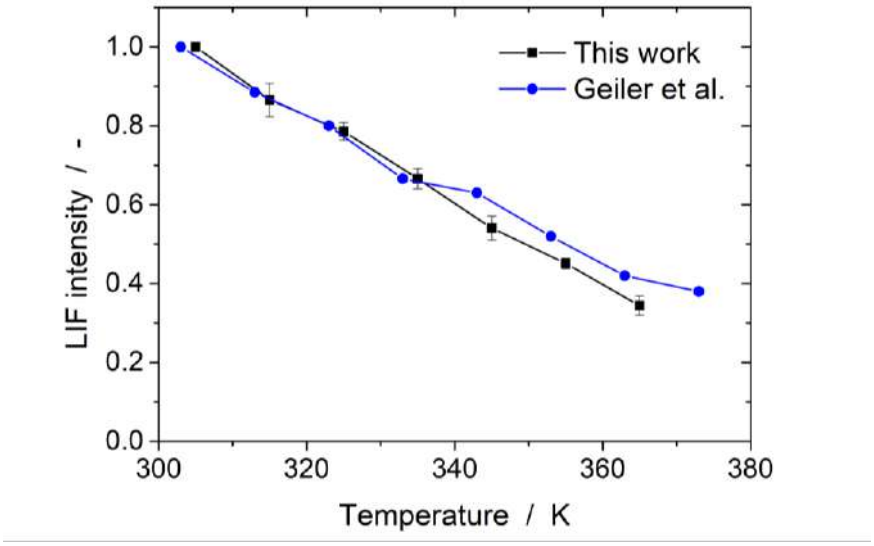

Figure 9: Temperature dependence of the LIF signal of liquid toluene[1].

Geiler *et al.* measured a decrease in the LIF signal about a factor of 2.6 from 303 to 373 K [1]. Note that the signals were normalized to the signal at 305 and 303 K for this work and the work from Geiler *et al*. A deviation of the liquid film's temperature of 10 K relatively to the wall temperature would result in an error of 9% in the measured film thickness.

Precision and accuracy

The relative standard deviation between the calibration measurements is 5.2% and 1.5% for fuel films of 10 µm and 100 µm, respectively. For the calibration with 100 µm, the signal-to-noise ratio (SNR) is 34, indicating a spatial standard deviation of 3%. For the calibration with 10 µm, the SNR becomes 14.6. Assuming that the noise is shot noise dominated, for a fuel film of 1.5 µm thickness, which was chosen as a threshold in the image processing, the maximum precision uncertainty becomes 17.7%. Thus, the total precision uncertainty is between 1.5% and 18.4%. A micrometer screw was used to determine the thickness of the distance shims used for calibration. The manufacturer states its inaccuracy with +/- 1 µm, corresponding to 10% for 10 µm shims. A maximum inaccuracy of about 8% in the predicted film thickness is possible because of the temperature difference between the injector and the quartz wall of 9 K. If we assume the fuel film to quickly reach wall temperature, this error becomes negligible soon after aSOI. Therefore, the total inaccuracy is 9.4%.

Another possible error source when quantifying the fuel-film thickness is the effect of oxygen quenching in the liquid phase. This phenomenon is widely known from gas-phase LIF where the presence of oxygen strongly decreases the LIF signal due to collisional signal quenching [42]. The effect was recently also observed in the liquid phase. When illuminating a fuel film with a certain thickness constantly with UV laser light, the signal increased about a factor of five. This effect is shown for a fuel film of 100 µm thickness in Figure 10 shows the mean LIF signal of the fuel film after a certain number of laser shots. The signal has increased about a factor of five after about 1500 laser shots, comprising a time of 150 seconds. After that the signal remains approximately constant. Most probably, the laser energy, partially absorbed by the fuel film, leads to locally hot regions within the fuel film. In these regions the oxygen thermally degases from the liquid film and most probably forms gas bubbles. That leads to a reduced oxygen concentration, a reduced quenching rate and thus to a higher signal.

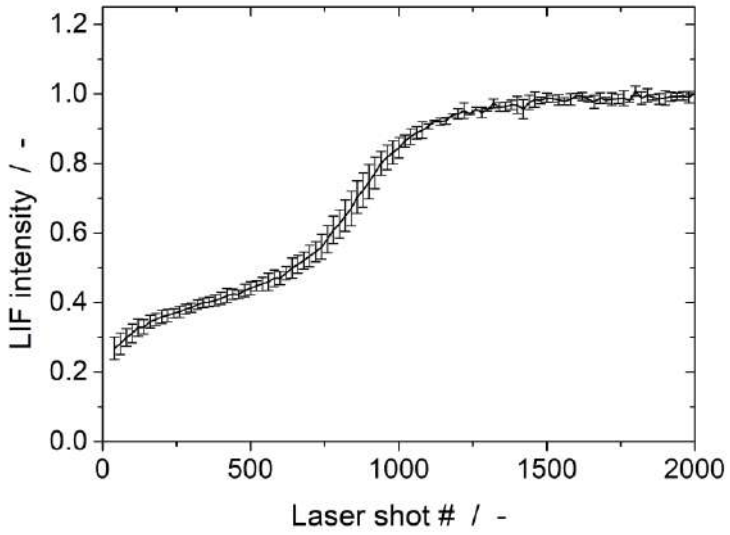

Figure 10: Effect of laser degassing on LIF signal of fuel film of 100 µm.

Since, in the actual measurement the fuel was injected with nitrogen as pressurized gas such that the liquid's film oxygen concentration might be different from that of the liquid film used for calibration. However, according to Figure 11, no significant difference in the LIF signal of the fuel films is detected after injection with either pressurized nitrogen or air. Here, the LIF signal of an individual fuel film was integrated along all pixels that exceed the thickness threshold of 1.5 µm. Figure 11 shows the accumulated LIF signals of one fuel film at different times aSOI until the film has completely evaporated. The data point "Flushed with air" was acquired after flushing the high-pressure injection system 5 times with air to enhance the bubbling of air through the fuel and eventually increase the oxygen concentration in the fuel. The results show that the deviations between the two curves are mostly within the indicated standard deviations. This implies that the oxygen concentration of the pressurized fuel does either not change with the type of pressurized gas or it immediately saturates with oxygen at ambient air pressure when propagating through the test section during injection. Also the flushing of air did not lead to a change in the accumulated LIF signal.

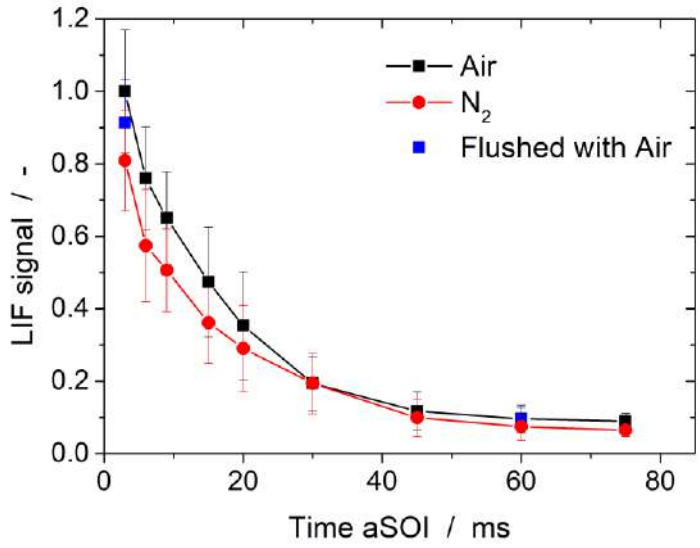

Figure 11: Accumulated LIF signal of fuel film 5 for air and nitrogen as pressurized gas at different times aSOI.

2.3.3 Fuel-vapour imaging

Figure 12 shows a plan view of the experiment for fuel vapour imaging. Here, a laser sheet formed a two-dimensional plane within the wind tunnel at 266 nm.

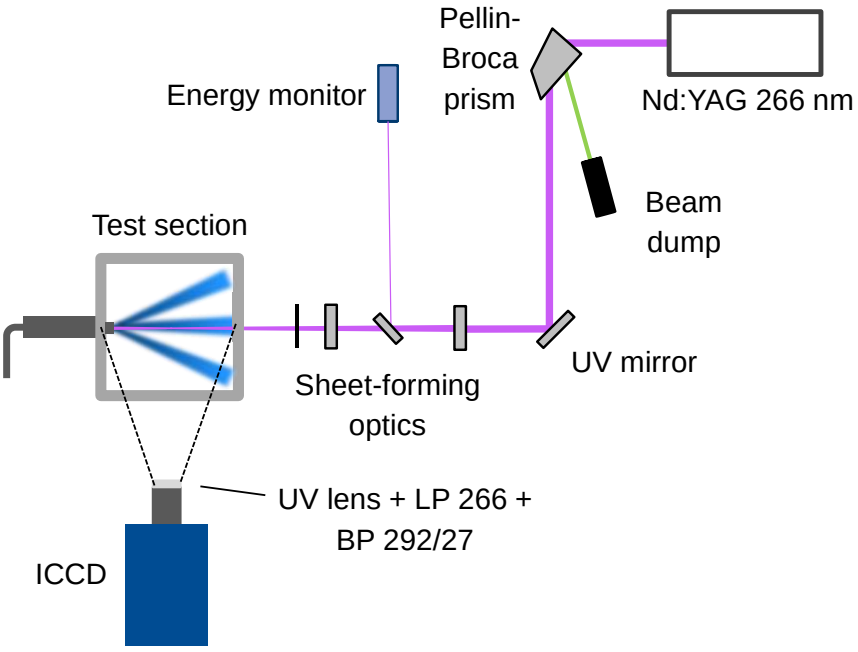

Figure 12: Optical layout for fuel-vapour LIF.

Again, the beam was directed towards the wind tunnel by the Pellin-Broca prism and mirrors. A positive cylindrical lens (f = 400 mm) focused the laser beam horizontally. A negative cylindrical lens (f = -25 mm) expanded the beam vertically into a light sheet. An aperture clipped the light sheet vertically. Horizontally, the sheet had a slight offset relatively to the centre plane of the test section to avoid shadowing by the electrodes. The intensified CCD camera was equipped with a UV lens (Cerco, f = 45 mm, f/1.8) and the same filter combination as for the fuel-film imaging. The projected pixel size was 0.15 mm/pixel. Again, the time between two images was long enough to flush the fuel vapour from the test section. The methodology, presented here, was applied to a previous injector before we were supplied with the project injector and with slightly different conditions than those indicated in Table 1. However, the same technique will be applied in Summer 2019 with the project injector at UDE.

Calibration of the fuel-vapour mole fraction versus the LIF signal and acquisition of a corresponding flat-field were done with the same arrangement. With the air heater switched off, i.e. at room temperature (T =294 K), the air flow through the wind tunnel was interrupted by inserting metal sheets into the top and bottom of the optically accessible section, as indicated on the left in Figure 13. A known mass of fuel was injected into the resulting closed volume and evaporated while a small fan in the lower part of the section increased the mixing of air and fuel vapour. The increase in total pressure and thus density due to the injected fuel was considered, while the effect of evaporative cooling was neglected. The temperature of the fuel/air-mixture was measured with a thermocouple in a preliminary investigation. With the highest fuel mole fraction of 0.063, the temperature of the charge shortly after the end of the last injection was about 5 K below ambient temperature. Within five seconds, which was also the minimum time between the last injection and the start of image acquisition, it was back to the ambient temperature again. This fast recovery is most probably due to two reasons. First, the fan increases convective heat transfer between the charge and the walls. Also, a significant part of the fuel evaporates from the walls and this does not contribute much to the evaporative cooling of the charge.

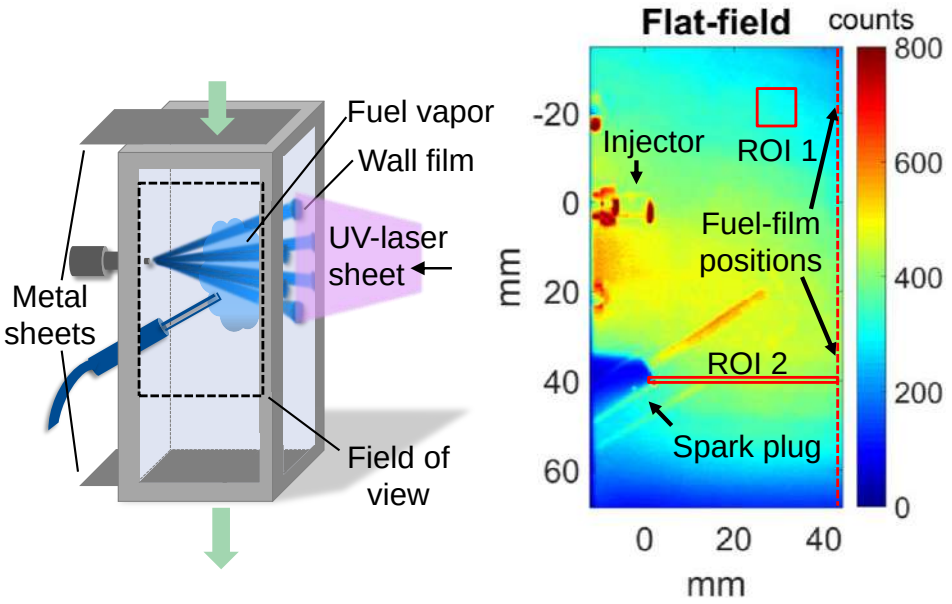

Figure 13: Flat-field acquisition: (left) covering the top and bottom of wind tunnel with metal sheets generates a closed volume, (right) ensemble average of 100 single shots after 15 injections into the resulting closed volume.

In the example image in Figure 13 the mole fraction of fuel is 2.7%. The laser sheet enters from the right. The dashed red line indicates the edge of the quartz wall and the black arrows point to the approximate location of the fuel films 1 and 4. The injector tip is at the origin of the coordinate system. The electrodes were slightly behind the illumination plane, but they blocked a small part of the laser sheet in the lower part of the image. High signal at the injector tip indicates some tip wetting. The high intensities close to the left wall stem from diffuse back reflections of the laser sheet and fluorescence from the nozzle and from bolts above and below the nozzle. The LIF intensity decreases towards the upper and lower edges of the image mainly because of the transverse intensity profile of the laser. Also, the field-dependent collection and detection efficiencies of the imaging system cause intensity gradients.

For checking if the LIF signal increases linearly with increasing fuel-vapour mole-fraction, the spatial mean of the LIF signal in a region of interest (ROI 1) was calculated for different mole fractions. Since the formation of soot close to the fuel-films is of interest, the ROI is chosen close to fuel film 1. Figure 14 shows the resulting curve. The coefficient of determination of the linear fit is 99%, indicating a very good approximation of the data points by the fit. Around a mole fraction of 3.5% the measured LIF signal does not follow the linear trend anymore. This is due to the fact that the saturation concentration of 4.9% (calculated from Dalton's law with T = 294 K) is approached and evaporation becomes slower. Therefore, the time between fuel injection and image acquisition was too short to evaporate the entire injected fuel. The LIF signal saturated at a mole fraction of about 5%, as expected. However, in the actual measurement the air temperature, which is also considered to be the fuel-vapour temperature, is 381 K and the saturation concentration is then 100%. Therefore, it was assumed that the linear relation between the LIF signal and the fuel-vapour mole-fraction applies up to 71% of the saturation concentration.

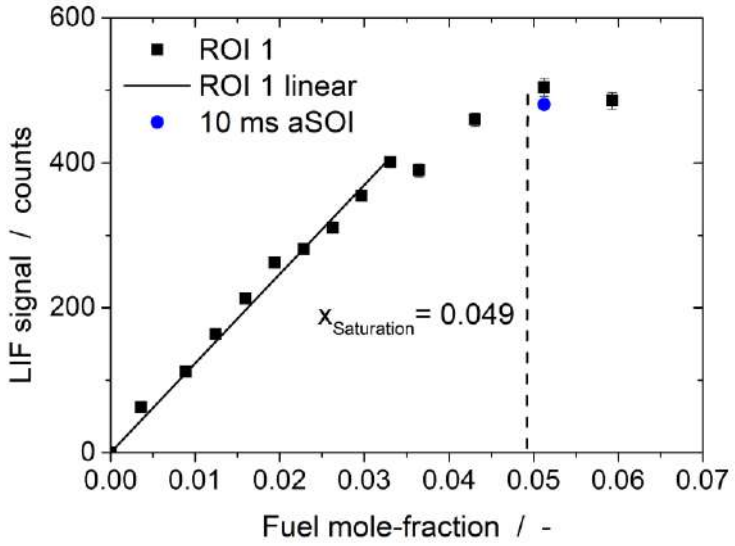

Figure 14: LIF signal versus fuel-vapour mole-fraction.

In a next step it was clarified that the non-linear relation between the LIF signal and the fuel concentration in Figure 14 does not stem from laser absorption in the gas phase. For this purpose, the LIF signal was vertically integrated in ROI 2, indicated in the lower part of the image in Figure 13 for the maximum investigated mole fraction of nominally 6.3%. The result is a clearly linear relation of the signal with increasing distance from right to left (graph not shown here), indicating that the non-linear relation in Figure 14 does not stem from laser absorption. This linear relationship over 4 cm path length can be expected. The 700 times lower density and the dilution with air in the test section lead to a 2500 times lower concentration of toluene in the fuel/air mixture than in the liquid fuel. Therefore, the absorption of the laser in a 4 cm thick mixture layer equals that in 16 µm of liquid fuel film.

To check for excessive absorption of the exciting laser sheet when passing through the fuel films on the quartz wall, an image was acquired during film evaporation 10 ms after start of injection at a mole fraction of 5%, see Figure 14. Significant absorption of the laser by the liquid would have led to a lower LIF signal than without the liquid on the wall. The LIF signal was only 4% lower at 10 ms aSOI than the signal without a fuel film.

The image processing of the fuel-vapour images is similar to that in fuel-film imaging. A background correction was applied to each acquired image. Pixel-wise multiplication of the corrected image with the fuel-vapour mole-fraction, according to Equation 8, results in the calibrated image:

$$x_{\mathrm{Fuel}}(x,y) = \frac{I_{\mathrm{f,exp}}(x,y)}{I_{\mathrm{f,FF}}(x,y)} \cdot x_{\mathrm{fuel,FF}} \cdot \frac{E_{\mathrm{Reference}}}{E_{\mathrm{Measured}}} \cdot \frac{I_f(298\ K)}{I_f(T_{\mathrm{Air}})} \tag{7}$$

Here, $I_{\mathrm{f,exp}}(x,y)$ is the background-corrected LIF intensity during the measurement and $I_{\mathrm{f,FF}}$ the background corrected flat-field intensity, which corresponds to the known fuel-vapour mole-fraction $x_{\mathrm{fuel,FF}}$. The difference in temperature of the toluene vapour in the calibration and in the measurement was taken into account by the ratio $\frac{I_{\mathrm{f}}(298\ K)}{I_{\mathrm{f}}(T_{\mathrm{Air}})}$, where $I_{\mathrm{f}}(298\ K)$ is the LIF signal of gaseous toluene at 298 K, and $I_{\mathrm{f}}(T_{\mathrm{Air}})$ that of gaseous toluene at air temperature. It was assumed that the fuel vapour is at the same temperature as the incoming air. The lowest possible temperature of the fuel vapour would arise if the injected fuel entirely evaporated within the hot air flow and the two species adiabatically mix. In that case, a fuel/air mixture with a fuel-vapour mole-fraction of 0.05 will have a temperature of about 337 K. Since the fuel first impinges on the hot quartz wall and then evaporates, the resulting fuel vapour temperature is unlikely to be the adiabatic

mixture temperature. The LIF signal of gaseous toluene in air is relatively insensitive to temperature (as opposed to the signal in nitrogen, which is strongly temperature dependent) [43]. Therefore, the error from temperature fluctuations throughout the field of view is small. The insensitivity against temperature variations originates from strong quenching by oxygen, the dominating depopulation mechanism of the excited state at these temperatures. The oxygen partial pressure was calculated to 0.19 bar when measuring a fuel-vapour mole-fraction of 0.1 and was 0.21 bar when acquiring the flat-field, resulting in different quenching efficiencies.

Precision and accuracy

The maximum precision uncertainty, dominated by shot noise, is 10.4% at a mole fraction of 0.4%. Inaccuracies in determining the fuel-vapour mole-fraction mainly stem from temperature fluctuations. Assuming that the temperature of the fuel-vapuor is bounded by the air temperature and the wall temperature ($\Delta T = 26$ K), results in a maximum inaccuracy of 7.6% in the fuel-vapour mole-fraction determination. When the fuel vapour approaches the adiabatic mixture temperature of 337 K of a fuel/air mixture with a fuel-vapour mole-fraction of 0.05, the resulting inaccuracy in determining the fuel-vapour mole-fraction would be 15.5%. The error from different magnitudes of oxygen quenching in measurement and flat-field acquisition is 9.5%. Measured fuel-vapour mole-fractions above 8.4% are presumably overestimated compared to actual mole fractions due to deviations from the linear relation between the LIF signal and the mole fraction.

2.3.4 Line-of-sight imaging

As complementary techniques, high-speed line-of-sight imaging of the spray and the natural flame luminosity and schlieren imaging of both film evaporation and flame luminosity were used. The experimental arrangement for Schlieren imaging is shown on the left in Figure 15. For schlieren imaging a blue LED (pulse width 5 µs) was used as a light source. To achieve a point-like light source and generate highly collimated light behind the collimator lens (f = 500 mm), an aperture clipped the image of the LED, produced by a condensing lens (f = 50 mm), to 0.7 mm in diameter. A mirror redirected the light towards the test section and the beam was focused by a second lens (f = 500 mm) onto a round aperture. A high-speed camera (Phantom V7.3) with a macro lens (Nikon, f = 105 mm, f/2.8) was exposed for 10 µs at 5000 frames per second. It needs to be taken into account schlieren imaging was done with an injector other than the project injector and also under slightly different experimental conditions than shown in Table 1.

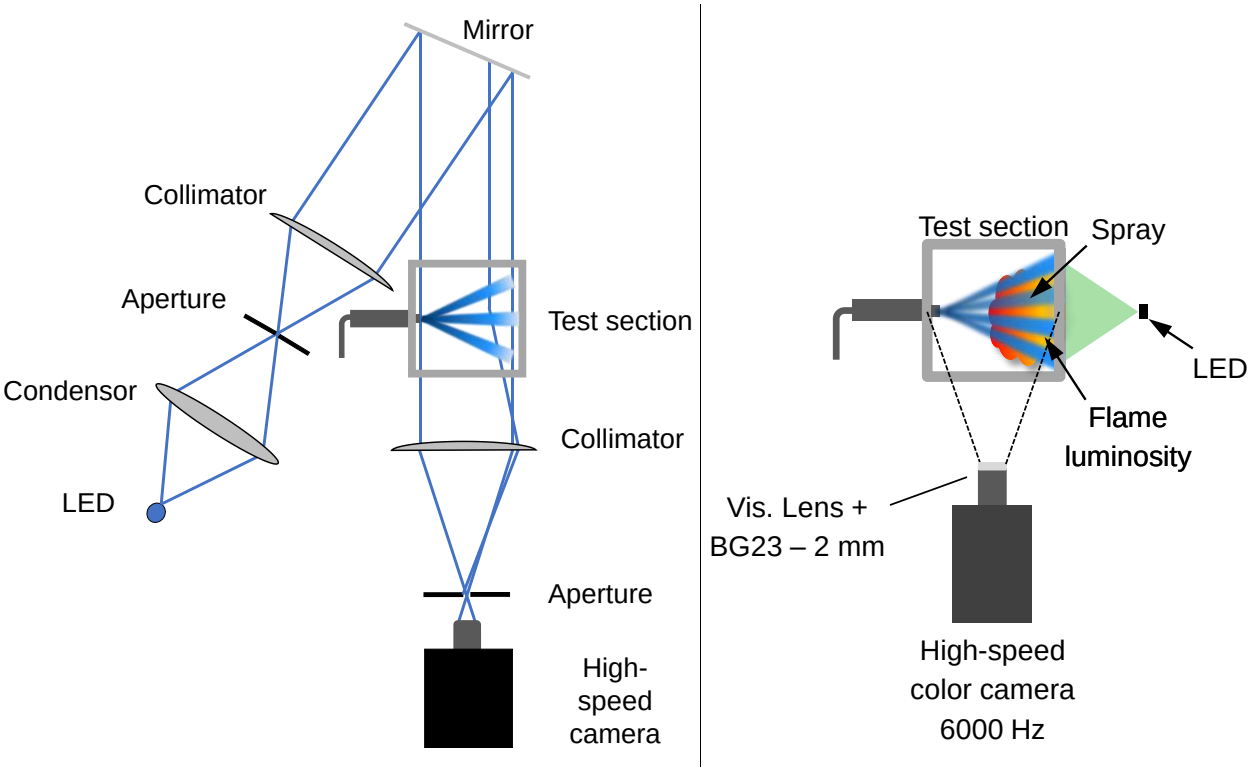

Figure 15: (left) Optical layout for schlieren imaging, (right) Optical layout for high-speed colour combustion-imaging.

The right hand side of Figure 15 shows the experimental setup for high-speed colour combustion-imaging. A high-speed colour camera (Phantom v1612), equipped with a lens (Nikon, f = 50 mm, f/1.8) and a bandpass filter (Schott, BG23, d = 2 mm) was used to visualize the spray, chemiluminescence, and natural soot incandescence. The filter was used to suppress the comparatively strong soot incandescence against the chemiluminescence. An LED illuminated the sprays and their impingement through the right wall. The LED was triggered for 5 µs and simultaneously with every image acquisition. The camera was focused on the centre plane of the test section and operated with an exposure of 124 µs at 6000 frames per second.

2.3.5 Soot and soot precursors

The layout for the simultaneous visualization of soot precursors (PAH) and soot is shown in Figure 16. A laser sheet at 532 nm was put into the test section to excite laser-induced fluorescence of PAH. A second laser sheet at 1064 nm was put into the test section to excite laser-induced incandescence of soot. Behind the output of the 532 nm laser, a Pellin-Broca prism separated remaining infrared light from the 532 nm beam and deflected the beam about 90°. A mirror reflected the 532 nm laser towards the test section. Two mirrors directed the 1064 nm beam towards the test section so that it had the same pathway as the 532 nm laser. A positive cylindrical lens (f = 400 mm) focused the laser beam horizontally. A negative cylindrical lens (f = -25 mm) expanded the beam vertically into a light sheet. An aperture clipped the light sheet vertically so that the two laser sheets opened up a two-dimensional with a height of 80 mm and a thickness of 0.5 mm. A beam splitter, BS509 (Semrock, Beamsplitter HC BS 509 imaging), transmitting light with a wavelength above 509 and reflecting light with a wavelength below 509 nm, was used to separate PAH LIF from soot LII. An intensified CCD camera, equipped with a lens (Nikon, f = 50 mm, f/1.8) and a bandpass filter, BP 435/40 (Semrock, 435/40 BrightLine HC), captured soot LII. The gate of the intensifier was set to 60 ns, starting with the laser pulse. A second intensified CCD camera, equipped with a lens (Nikon, f = 50 mm, f/1.8) and a bandpass filter (Schott, OG550), captured PAH LIF. Here, the gate of the intensifier was set to 30 ns, also starting with the laser pulse. The short gating suppressed the interference from natural flame luminosity. The temporal delay between the two laser pulses was 500 ns so that a quasi-simultaneous visualization was performed. The projected pixel size was 0.14 mm/pixel. The time between two images was 2.5 seconds.

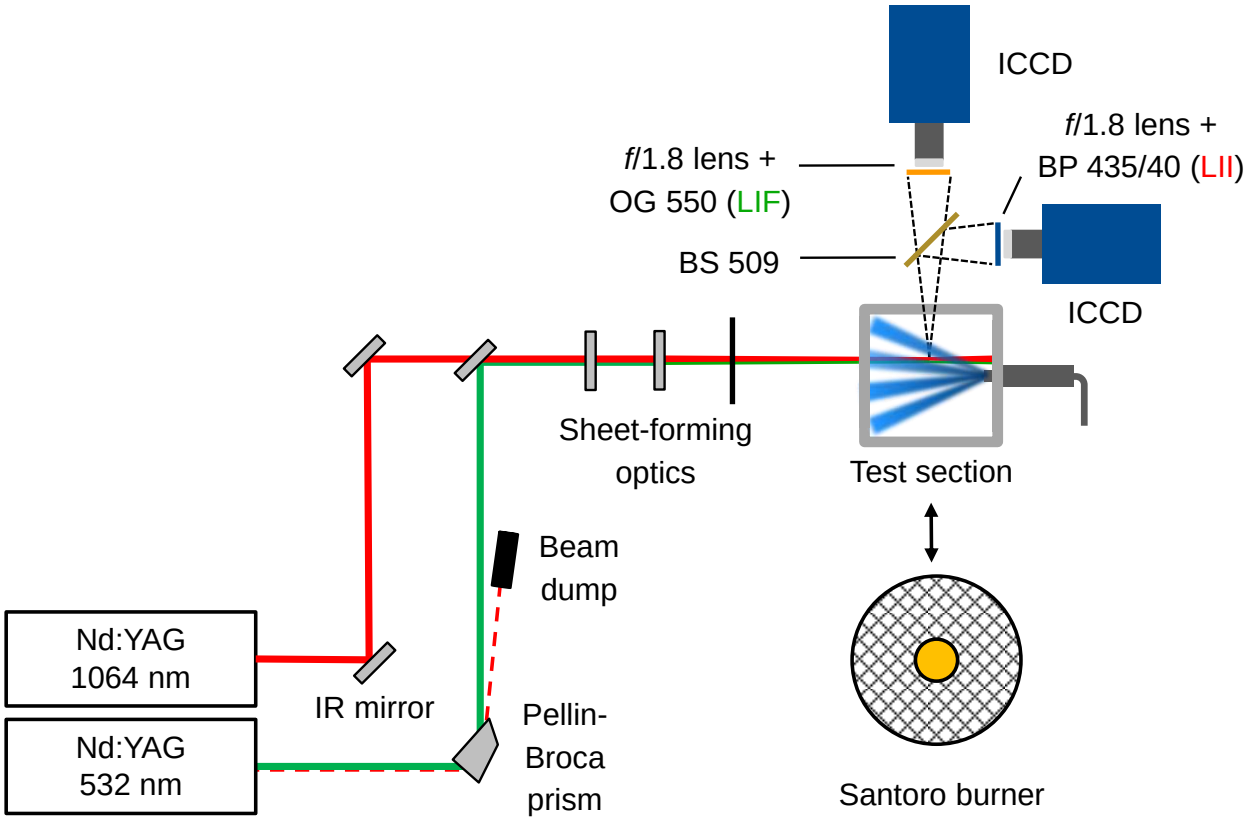

Figure 16: Optical layout for PAH LIF and soot LII.

The test section was replaced by a burner (Santoro burner), providing a stationary sooting, laminar diffusion flame. The flame was used to perform in-situ preliminary measurements. First, the dependence of the LII signal versus the laser fluence was investigated. Second, the applicability of the measurement technique to simultaneously visualize PAH and soot was successfully tested. Third, the burner flame was used to calibrate the LII signal against the soot volume fraction. The experimental setup of the Santoro burner is shown in Figure 17. It consists of two concentric nozzles. The inner nozzle has an inner diameter of 10 mm and was fed with a volume flow of 0.231 l/min of ethylene. The outer nozzle is a honeycomb that provided an air co-flow with a volume flow of 43 l/min.

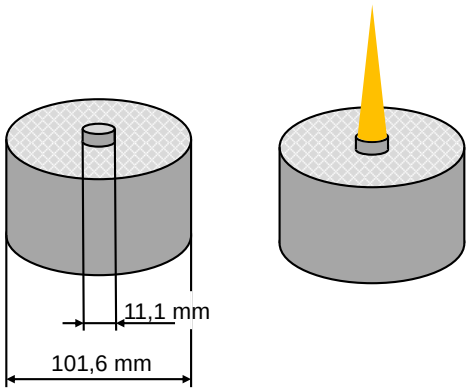

Figure 17: Experimental setup of Santoro burner.

Figure 18 shows the spectrum of PAH LIF excited at 532 nm from a laminar diffusion flame [24]. A notch filter blocked laser stray light at 532 nm, explaining the lack of signal in that region. Assuming that the laser sheet heats the soot particles to its sublimation temperature of about 4000 K, depending on the specific material properties of soot, and regarding soot as a blackbody, results according to Planck's law in the emission spectrum "LII 4000 K". Also shown are the transmission spectra of the beam splitter BS509 and the two